Applied Catalysis B: Environmental 132–133 (2013) 416–422

Contents lists available at SciVerse ScienceDirect

Applied Catalysis B: Environmental

journal homepage: www.elsevier.com/locate/apcatb

# Halloysite–$TiO_2$ nanocomposites: Synthesis, characterization and photocatalytic activity

Dimitrios Papoulis[a,*], Sridhar Komarneni[b], Dionisios Panagiotaras[c], Elias Stathatos[d], Despina Toli[a], Konstantinos C. Christoforidis[e], Marcos Fernández-García[e], Huihui Li[f], Shu Yin[f], Tsugio Sato[f], Hiroaki Katsuki[g]

[a] Department of Geology, University of Patras, 26504, Patras, Greece
[b] Materials Research Institute, 205 Materials Research Laboratory, The Pennsylvania State University, University Park, PA 16802, USA
[c] Department of Mechanical Engineering, Technological Educational Institute of Patras, 26334, Patras, Greece
[d] Electrical Engineering Department, Technological-Educational Institute of Patras, GR-26334 Patras, Greece
[e] Instituto de Catálisis y Petroleoquímica, CSIC, C/ Marie Curie 2, 28049 Madrid, Spain
[f] Institute of Multidisciplinary Research for Advanced Materials, Tohoku University, Sendai 980-8577, Japan
[g] Saga Ceramics Research Laboratory, 3037-7, Arita-machi, Saga, 844-0022, Japan

ARTICLE INFO

*Article history:*
Received 10 September 2012
Received in revised form 3 December 2012
Accepted 7 December 2012
Available online 20 December 2012

*Keywords:*
Halloysite
Titania
Nanocomposite
Photocatalytic activity

ABSTRACT

Two halloysite–$TiO_2$ nanocomposites were prepared with two different tubular halloysite clays by depositing anatase-$TiO_2$ on the halloysite surfaces using titanium isopropoxide under hydrothermal treatment at 180 °C. The nanocomposites were characterized by X-Ray diffraction (XRD), transmission electron microscopy (TEM), scanning electron microscopy (SEM), attenuated total reflection using Fourier transform infrared spectroscopy (ATR-FTIR), absorption properties by UV–vis spectroscopy and $N_2$ specific surface area (SSA) analysis by BET method. Good dispersion of 3–10 nm $TiO_2$ particles on halloysite external surfaces was achieved in both the halloysite–$TiO_2$ nanocomposites and ATR-FTIR results showed the formation of hydrogen bonding between $TiO_2$ and the outer surfaces of halloysite tubes. After treating with $TiO_2$, both halloysite samples largely showed interparticle mesopores of about 5.7 nm. However, the macropores of halloysite (lumen or central hole in halloysite tubes) were not detected probably as a result of plugging of the lumens in halloysite tubes by $TiO_2$ nanoparticles. These nanocomposites were tested for their photocatalytic activities in decomposing $NO_x$ gas and toluene. The halloysite–titania samples showed significantly higher activity in decomposing $NO_x$ gas under visible-light irradiation ($\lambda > 510$ nm) and UV–visible light irradiation ($\lambda > 290$ nm) compared to that of the standard commercial titania photocatalyst, P25. In addition, composite photocatalyst showed larger catalytic activity either under sunlight or pure UV irradiation in decomposing toluene compared to the commercial titania, P25. Our experimental data suggest that the enhanced photocatalytic activity is related with the good dispersion of the $TiO_2$ nanocrystals on the surface of the clay minerals.



## 1. Introduction

In the last few decades, enormous efforts have been devoted to the research of oxide semiconductor photocatalysts with high activities for environmental protection [1–4]. Among various semiconductors $TiO_2$ is extensively used mainly because of its high effectiveness, stability and nontoxicity [3,5–7]. It is well known that ultra fine $TiO_2$ powders, especially in the form of anatase have good catalytic activities because of their large specific surface areas where reactions take place [8] but in some cases combination with a small fraction of rutile have also shown excellent photocatalytic activities (e.g. Degussa-P25). Titanium dioxide has proven to be the most suitable semiconductor for widespread environmental applications such us the degradation of oil spills and the decomposition of many organic and as well as air pollutants [9–13]. However, $TiO_2$ powders easily agglomerate into larger particles, reducing their performance [8]. $TiO_2$ in pillared clays showed improved photocatalytic activities in decomposing air and organic pollutants [14–16].

In aqueous dispersions, clay minerals have been used in combination with $TiO_2$ to enhance the removal of organic pollutants by photocatalytic degradation [17–19]. Additionally, many clay minerals have been used in combination with $TiO_2$ in order to increase the photocatalytic activities in decomposing $NO_x$ gas [16,20–22]. Previous experiments showed that using clay minerals with microfibrous [23,24] or tubular morphology [21,25] increased $TiO_2$ photocatalytic activity. Recent studies revealed that dispersing

* Corresponding author. Tel.: +30 2610 997842; fax: +30 2610997560.
*E-mail address:* papoulis@upatras.gr (D. Papoulis).

0926-3373/$ – see front matter © 2012 Elsevier B.V. All rights reserved.
http://dx.doi.org/10.1016/j.apcatb.2012.12.012

the $TiO_2$ particles onto clay mineral's surfaces under mild conditions is a promising method to resolve the agglomeration problem of $TiO_2$ [21,26].

In present work, we describe the synthesis, characterization and photocatalytic activities of nano-sized $TiO_2$ particles supported on two different halloysites by using a novel method under mild conditions. This method does not require stabilizing agents or calcination. We performed an evaluation of their photocatalytic efficiency using UV or visible light, against inorganic and organic air pollutants: (i) in decomposing $NO_x$ gas an important air pollutant which contributes to the formation of acid rain and to stratospheric ozone destruction; (ii) in toluene vapor photo-elimination, one of the most prevalent and harmful volatile organic compounds typical of urban atmospheres [27].

## 2. Materials and methods

### 2.1. Sample preparation

A halloysite sample from Limnos island, Greece and another halloysite sample from Utah, USA were used. The samples were size fractionated to obtain <2 μm by gravity sedimentation. Separation of the clay fraction was carried out by using centrifugation methods. The clay fractions of the most halloysite-rich samples were used for the preparation of $TiO_2$–halloysite nanocomposites. Both halloysites are pure, well crystallized and dehydrated halloysites with tubular morphology. The tubes of halloysite from Limnos island are better formed than halloysite from Utah.

### 2.2. $TiO_2$ stock sol dispersion

A stock $TiO_2$ sol dispersion was prepared by mixing titanium tetraisopropoxide, $Ti(OC_3H_7)_4$, with hydrochloric acid, nanopure water and absolute ethanol [28]. The $TiO_2$ stock dispersion was diluted in absolute ethanol to give a 0.05 M concentration of $Ti(OC_3H_7)_4$.

### 2.3. Halloysite-supported $TiO_2$

An aliquot of $TiO_2$ sol was stirred for 2 h and the (1% w/w) halloysite-water dispersion was added to the dispersion in order to obtain a final $TiO_2$ content of 70% w/w. The slurry was stirred for 24 h and the resulting dispersion was centrifuged for 10 min (3800 rpm) followed by three times centrifuge washing with triple distilled water. The halloysite–$TiO_2$ composite was then dispersed in a 1:1 water:ethanol solution, prior to hydrothermal treatment in an autoclave for 5 h at 180 °C. The products were centrifuged for 15 min (at 3800 rpm) and oven-dried for 3 h (at 60 °C). The obtained halloysite–$TiO_2$ nanocomposites from Greece and USA are hereinafter designated as samples Ti–Hal1 and Ti–Hal2, respectively.

### 2.4. Characterization

The phase compositions of untreated and $TiO_2$ treated halloysite samples were determined by X-ray diffraction (using a Bruker D8 advance diffractometer, with Ni-filtered CuKα radiation). XRD patterns were obtained from oriented or random powder samples in a $2\theta$ range of 2°–60° at a scanning rate of 2°/min. Random powder mounts for selected samples were prepared by gently pressing the powder into the cavity holder. Oriented clay powder samples were prepared by the dropper method.

Halloysite–$TiO_2$ morphology and chemical composition were examined with a SEM LEO SUPRA 35VP. The morphology of the samples was also determined by transmission electron microscopy (TEM; Model 2010, JEOL, Tokyo, Japan).Attenuated total reflection infrared (ATR/FTIR) measurements were made with the ATR Miracle accessory of PIKE technologies (diamond crystal) attached to the EQUINOX 55 FT-IR spectrometer (BRUKER). ATR-FTIR spectroscopy is suitable for characterization of materials which are either too thick or too strongly absorbing to be analyzed by TEM and therefore no sample preparation is required.

Nitrogen adsorption–desorption isotherms for each sample degassed at 100 °C for 3 h were obtained at 77 K using Autosorb$^{-1}$ (Quantachrome corporation). Brunauner–Emmet–Teller (BET) surface areas and pore size distribution were determined from the isotherms. Pore size distribution of each sample was obtained using density functional theory (DFT) method in which a $N_2$ adsorption branch model was selected. The ultraviolet visible diffuse reflectance spectrum was taken by a UV–vis spectrophotometer (Shimadzu, UV-2450).

The photocatalytic activity for nitrogen monoxide destruction was determined by measuring the concentration of NO gas at the outlet of the reactor (373 $cm^3$ of internal volume) during the light irradiation of constant flowed 1 ppm NO-50 vol.% air mixed (balance $N_2$) gas (200 $cm^3$/min). The photocatalyst (ca. 0.04 g) was placed in a hollow place of 20 mm × 15 mm × 0.5 mm on a glass holder/plate and set in the center of the reactor. The photocatalyst under test was first equilibrated with the flowing NO gas before turning on the light. A 450 W high-pressure mercury arc lamp was used as the light source. The wavelength was controlled by selecting filters, i.e., Pyrex glass for >290 nm, Kenko L41 Super Pro (W) filter >400 nm and Fuji triacetyl cellulose filter >510 nm. The concentration of NO was determined using a $NO_x$ analyzer (Yanaco, ECL-88A). It has been reported that during the photocatalytic destruction, about 20% of NO is directly reduced to $N_2$, and the other 80% is oxidized to $NO_3$-species [29]. For comparison, the photocatalytic reaction was also carried out using the standard commercial titania (Degussa P25).

Activity and selectivity for the gas-phase photo-oxidation of toluene were tested in a continuous flow annular photoreactor [30,31] containing ca. 40 mg of photocatalyst as a thin layer coating on a pyrex tube. The corresponding amount of catalyst was suspended in 1 ml of ethanol, painted on a pyrex tube (cut-off at ca. 290 nm) and dried at room temperature. The reacting mixture (100 ml/min) was prepared by injecting toluene (Panreac, spectroscopic grade) into a wet (ca. 75% relative humidity) 20 vol.% $O_2/N_2$ flow before entering at room temperature to the photoreactor, yielding an organic inlet concentration of ca. 800 ppmv. After flowing the mixture for 3–4 h in the dark (control test), the catalyst was irradiated by four lamps symmetrically positioned outside the photoreactor. The photocatalytic tests were performed under pure UV-light irradiation (Philips TL 6W/08) as well as under a radiation spectrum simulating sunlight (Philips TL 6W/54-765). Reaction rates (measured as toluene disappearance) were evaluated under steady state conditions, typically achieved after 4–5 h from the beginning of irradiation. No change in activity was detected for all samples within 24 h after reaching steady state conditions. In all cases studied, the *C* balance was more than 97%. The concentration of reactants and products was analyzed using an on-line gas chromatograph (Agilent GC 6890) equipped with HP-PLOT-Q/HP-Innowax columns (0.5/0.32 mm I.D. × 30 m) and TCD/FID detectors for the quantification of $CO_2$ and organic substances (toluene, photocatalytic products), respectively. The catalytic reactions were conducted in duplicate.

## 3. Results and discussion

### 3.1. X-ray diffraction

Both halloysite samples are almost pure with very low amounts of impurities if any (not detected by XRD), as it has been reported

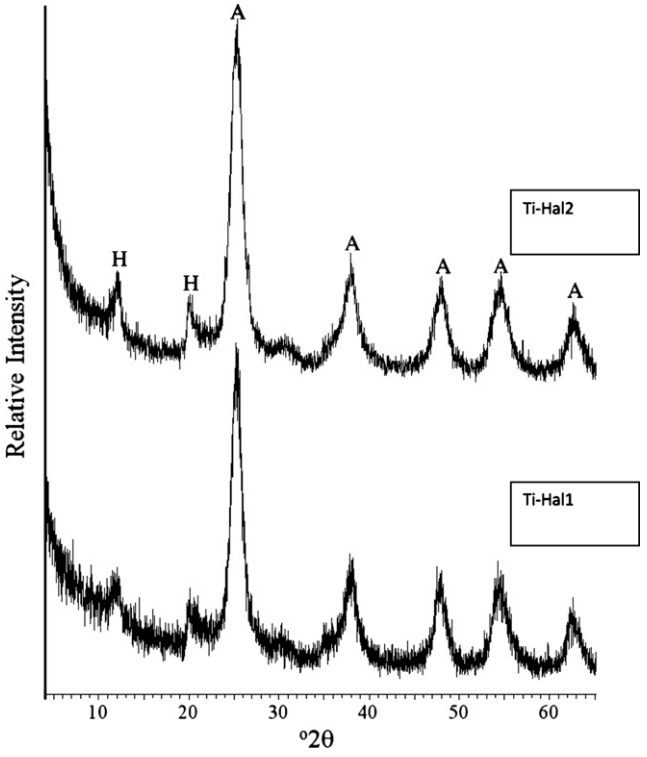


**Fig. 1.** XRD patterns of Ti–Hal1 and Ti–Hal2 (H: Halloysite, A: Anatase).

in previous studies [21]. Fig. 1 shows the XRD patterns of the nanocomposites (Ti–Hal1 and Ti–Hal2). Both patterns are characterized only by the presence of the minerals halloysite and anatase confirming their purity. These two patterns are similar while the basal reflections of both halloysites are significantly smaller than anatase reflections. The XRD patterns of both nanocomposites exhibited all the characteristic reflections of anatase ($\gamma$-$TiO_2$) at 25.3°, 37.9°, 47.6°, 54.8° 2$\theta$. It is therefore concluded that the temperature (180 °C) involved in the synthesis did not modify the native dehydrated halloysite mineral structure. It is well known [32,33] that heating halloysite at 100–350 °C sharpens the basal reflection and reduces the spacing, in our case to 7.29 Å (Fig. 1), but never to as low as the characteristic reflection of kaolinite (7.14 Å).

### 3.2. ATR-FTIR spectra

The ATR-FTIR spectra of halloysites and $TiO_2$-treated halloysites are generally similar (Fig. 2a, b), while the intensities of halloysite reflections are lower in the nanocomposites because of the lower amounts of halloysite (30%) in them. The reflections of the spectra

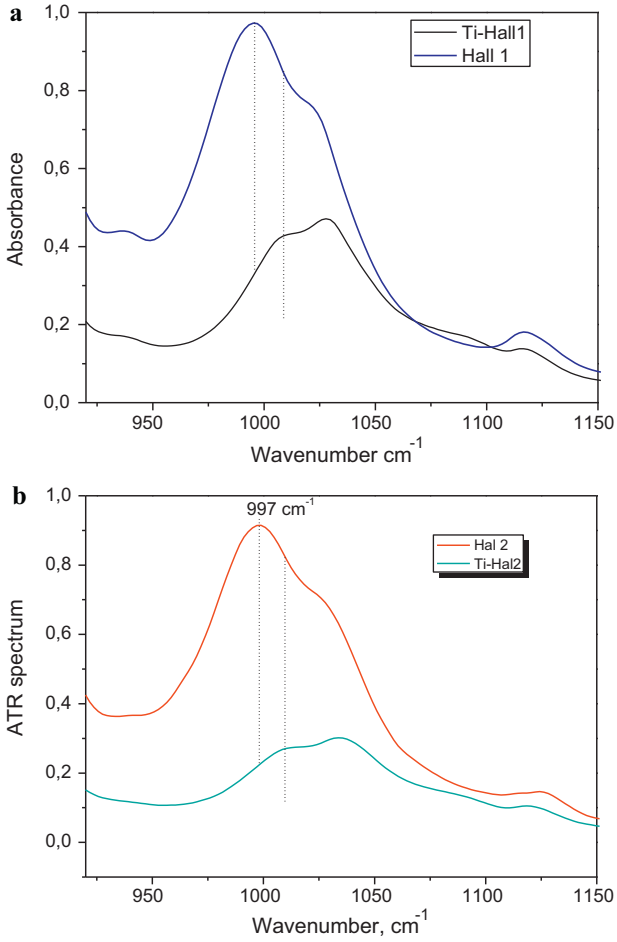


**Fig. 2.** ATR-FTIR spectra showing the characteristic Si—O broad stretching band that appears at about 997 $cm^{-1}$ in halloysites which shifted for both (a) Ti–Hal1 and (b) Ti–Hal2 to about 1011 $cm^{-1}$.

show that the structures of both halloysites were not changed after treating with $TiO_2$. None of the characteristic bands of dehydrated halloysite [33,34] are affected except from the Si–O broad stretching band that appears at about 997 $cm^{-1}$ which shifted for both nanocomposites to about 1011 $cm^{-1}$ (Fig. 2a, b). The shifting of the Si—O broad stretching band indicates the formation of hydrogen bonding between $TiO_2$ and the outer surfaces of halloysite tubes (tetrahedral sheet) [21]. ATR-FTIR confirmed that the treatment temperature of 180 °C involved in the synthesis did not destroy halloysites, or modify their native dehydrated halloysite mineral structure.

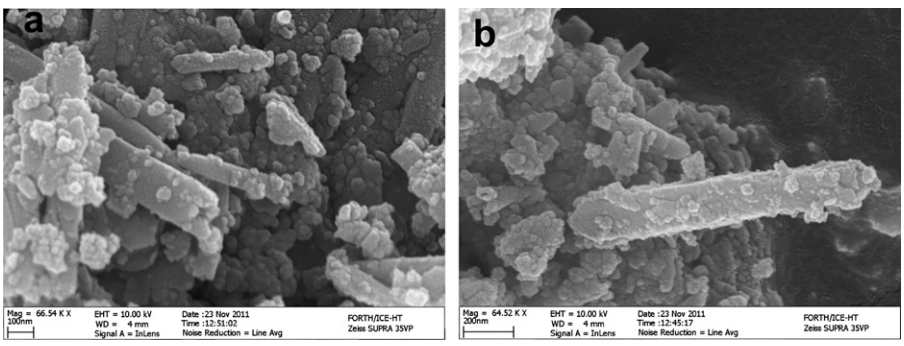


**Fig. 3.** SEM micrographs of samples: (a) Ti–Hal1 and (b) Ti–Hal2.

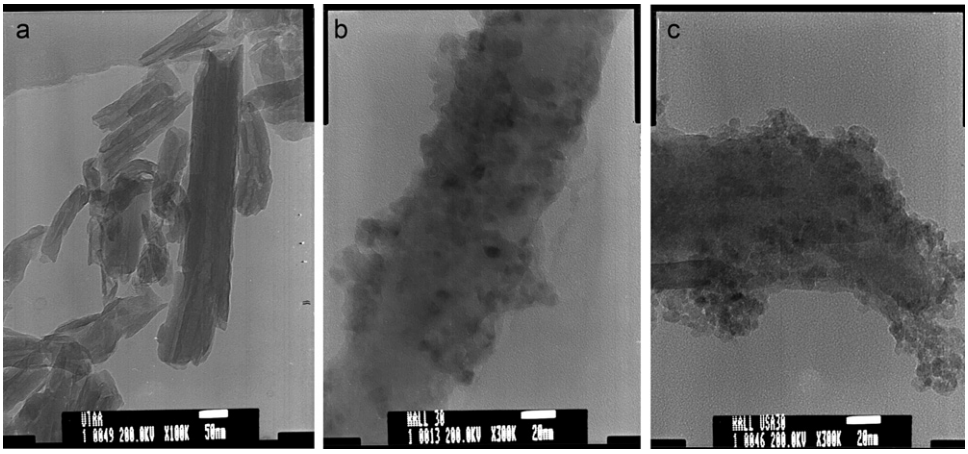


**Fig. 4.** TEM images of samples (a) Halloysite from Utah (b) Ti–Hal1 and (c) Ti–Hal2 showing well dispersed 3–10 nm $TiO_2$ particles on halloysite tubes (b, c).

### 3.3. Scanning electron microscopy (SEM) and transmission electron microscopy (TEM)

The morphology of both halloysites has already been presented in previous work [21]. Therefore, in this paper we present SEM micrographs of nanocomposites, Ti–Hal1 and Ti–Hal2 (Fig. 3). SEM observations of nanocomposites revealed that many uniform $TiO_2$ grains of about 10–30 nm were deposited on the halloysite tubes (Fig. 3a, b). The homogeneous distribution of $TiO_2$ grains on halloysite tubes is anticipated in order to improve the properties and potential uses of the prepared nanocomposites. The deposited $TiO_2$ nanoparticles were found to be distributed very well on halloysite surfaces (Fig. 3), but not homogeneously. $TiO_2$ nanoparticles tend to cover the lumen of most halloysite tubes and appear to have been deposited at least partially within the lumen as observed by TEM (Fig. 4). TEM observations confirm that $TiO_2$ particles are well dispersed on halloysite tubes but also revealed that their grain size varied from 3–10 nm (Fig. 4a, b). The latter shows that $TiO_2$ grain size observed by TEM is significantly lower than that observed by SEM. This is due to the relatively (compared with TEM) low resolution of SEM which could not allow us to discriminate the (3–10 nm) $TiO_2$ nanoparticles. We found significant differences in the morphology of halloysite tubes between the two halloysites were used. The halloysite tubes from Limnos island appear to be well formed [21], while those from Utah are not curved and rolled up that perfectly (Fig. 4a). As a result, there are more halloysite surfaces available for $TiO_2$ nanoparticles to be dispersed in the sample from Utah.

### 3.4. Determination of specific surface area and porosity

Adsorption–desorption isotherms of nitrogen and pore size distributions for $TiO_2$-treated halloysites are presented in Figs. 5 and 6 respectively. The isotherm shapes for both nanocomposites are similar (type IV) indicating both meso and micropores (IUPAC classification) [35,36]. The total pore volume of the Ti–Hal1 was found to be significantly higher while the specific surface area was found to be slightly smaller than the Ti–Hal2 (Table 1, Fig. 6). This could be attributed to the presence of more interparticle pores (macroporous) of sample Ti–Hal1 while the sample Ti–Hal2 showed more mesoporous pores at about 5.7 nm (Fig. 6) and retained the higher SSA due to a better $TiO_2$ distribution on halloysite tubes. The above observation is supported by the pore size distribution data (Fig. 6, Table 1). Both nanocomposites largely showed mesopores of about 5.7 nm, while the macropores found in starting halloysite material (observed in previous papers [21]), especially for Ti–Hal2 are significantly reduced. The latter is probably due to the covering of the lumen of halloysite tubes by $TiO_2$ nanoparticles, as SEM and TEM observations have already shown, and this could also be the reason why the pore sizes of the $TiO_2$-treated halloysites are significantly smaller (Table 1).

### 3.5. Photocatalytic activity of selected gases

The photocatalytic activities of both nanocomposites in decomposing $NO_x$ gas are plotted in Fig. 7a. The prepared halloysite–$TiO_2$ samples showed significantly higher activity under visible-light irradiation ($\lambda > 510$ nm), up to 9.38 times and under UV–visible light irradiation ($\lambda > 290$ nm), up to 1.69 times than that of the commercial titania, P25. On a total $TiO_2$ mass basis (Fig. 7b), halloysite–$TiO_2$ nanocomposites are exceptionally better than standard titania i.e., up to 13.4 times under visible-light irradiation ($\lambda > 510$ nm), and up to 2.4 times under UV–visible light irradiation ($\lambda > 290$ nm), than that of the commercial titania, P25. It should be noted that the most efficient photocatalyst is the one with halloysite from Utah especially under visible-light irradiation. The other photocatalyst

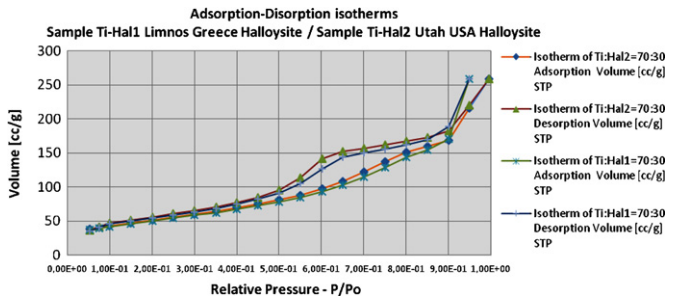


**Fig. 5.** Adsorption–desorption isotherms of nitrogen for Ti–Hal1 and Ti–Hal2.

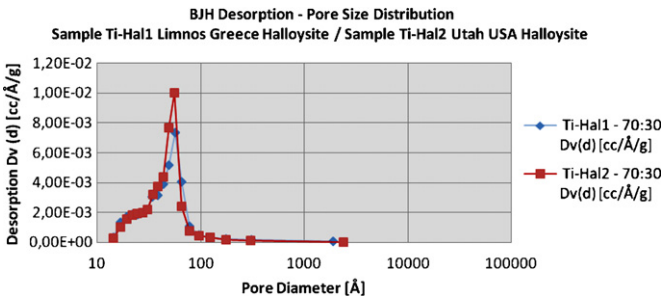


**Fig. 6.** Pore size distribution for Ti–Hal1 and Ti–Hal2.

**Table 1**
Basal spacing ($d_{001}$), pore volume, specific surface area (SBET) and $TiO_2$ content.

| Sample | Basal Spacing d (0 0 1) | (Total) Pore volume (mL/g) at $P/P_o = 0.99$ | Pore volume (mL/g) at $P/P_o = 0.95$ | SBET ($m^2$/g) | $TiO_2$ content (wt.%) |
|---|---|---|---|---|---|
| Hal1 | 7.41 | 0.44 | 0.117 | 38 | 0 |
| Ti–Hal1 | 7.29 | 0.40 | 0.279 | 183 | 70 |
| Hal2 | 7.40 | 0.29 | 0.163 | 47 | 0 |
| Ti–Hal2 | 7.29 | 0.34 | 0.277 | 187 | 70 |

Based on repeated adsorption measurements, the estimated errors for pore volume and SBET values of our instrument are lower than ±1%.

(Ti–Hal1) also showed high values in decomposing $NO_x$ gas compared to P25 under both visible-light and UV irradiation (6.56 and 1.65 respectively) but not as high as the first one (using halloysite from Utah). Catalytic tests were also performed on both untreated halloysite samples which served as controls and they showed no photocatalytic activity in the destruction of $NO_x$ and decomposition of toluene, as expected.

In addition, Fig. 8 presents steady state reaction rates of toluene gas-phase photocatalytic oxidation by the two Halloysite–$TiO_2$ catalysts obtained under pure UV (circles) and sunlight irradiation (squares). The photo-catalytic data are presented based on the total catalyst weight, i.e., halloysite + $TiO_2$ (Fig. 8a) as well as based on the $TiO_2$ content (Fig. 8b). For comparison, the photocatalytic parameters obtained for commercial Degussa P25 are also included.

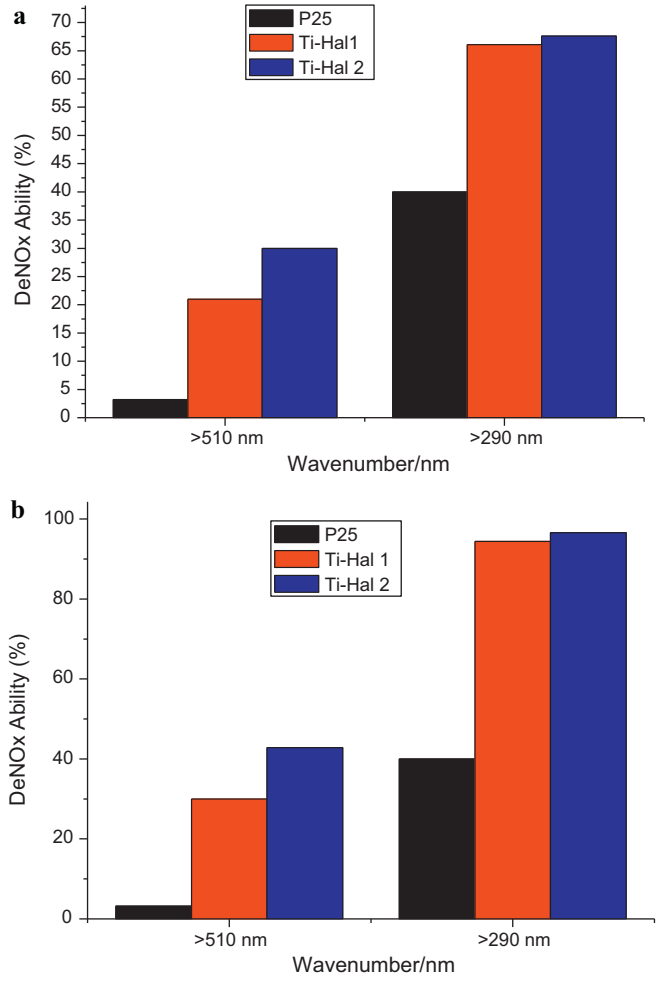


**Fig. 7.** (a) Photocatalytic activities in decomposing $NO_x$ gas by commercial titania P25, $TiO_2$-treated halloysite (Ti–Hal1) and $TiO_2$-treated halloysite (Ti–Hal2), (b) Photocatalytic activities in decomposing $NO_x$ gas by commercial titania P25, $TiO_2$-treated halloysite (Ti–Hal1) and $TiO_2$-treated halloysite (Ti–Hal2) based on $TiO_2$ content.

Under both UV and sunlight irradiation, both halloysite-supported $TiO_2$ samples showed larger catalytic activity compared to the commercial titania, P25. Catalytic tests carried out in the dark confirmed that the measured activities were fully attributable to photo-induced processes. The photocatalytic performance of

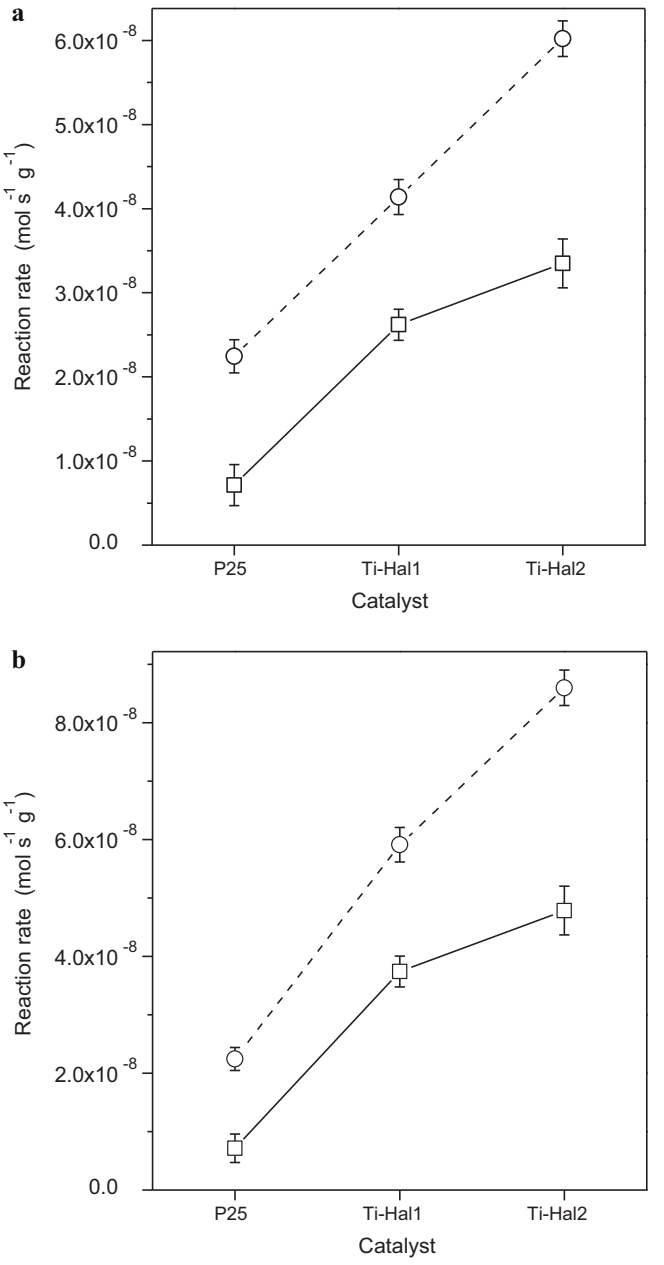


**Fig. 8.** Steady state reaction rates of toluene gas-phase photocatalytic oxidation by commercial titania P25 and $TiO_2$-treated halloysite (Ti–Hal1 and Ti–Hal2) under pure UV (○) and sunlight (□) irradiation based on (a) total catalyst's content ($TiO_2$ + halloysite) and (b) $TiO_2$ content.

the $TiO_2$–halloysite nanocomposites was found to be even better when compared to standard commercial titania on the basis of $TiO_2$ content (Fig. 8b). The higher reaction rates corresponded to the Ti–Hal2 sample. The reaction rates of toluene photo-oxidation by the Ti–Hal2 sample were 3.8 and 6.7 times greater compared to that of P25 under pure UV and sunlight irradiation respectively, taking into account the Ti-content of the materials (Fig. 8b). The Ti–Hal1 sample presented also increased photo-activity compared to that of P25, i.e. 2.63 and 5.26 times larger under pure UV and sunlight irradiation, respectively (Fig. 8b).

The reaction products of the catalytic tests were also checked. Under the experimental conditions of the present study, the reaction products detected during toluene photo-oxidation were $CO_2$ and benzaldehyde, in agreement with previous results using similar [26] or other $TiO_2$-based systems [31]. Both halloysite-supported $TiO_2$ samples showed higher formation of total oxidation products (62 and 66% $CO_2$ yields for the Ti–Hal1 and Ti–Hal2 respectively) compared to the commercial titatia P25 (29% $CO_2$ yield).

The higher photocatalytic activity of the Ti–Hal2 sample compared to the Ti–Hal1 could be attributed to its higher SSA despite its lower total pore volume because the target pollutants are in gas phase. The higher pore volume of the Ti–Hal1 sample is due to relatively large pores representing halloysite interparticle porosity and halloysite's lumens. Halloysite's interparticle porosity has no positive effect on photocatalytic activity (even though it results in an increase of SSA) while halloysite's unblocked lumen indicates poorer $TiO_2$ dispersion on halloysite tubes, as corroborated by the TEM micrographs. The latter explains the relatively higher photocatalytic activity of photocatalyst with halloysite from Utah (i.e. Ti–Hal2). It should also be noted that the halloysite's interparticle porosity of the Ti–Hal1 sample, which results in an increase of the SSA but with no positive effect on photocatalytic activity, is the reason why the SSA value of the sample with halloysite from Utah is not much higher than the SSA of the Greek sample. Additionally and more importantly the halloysite tubes from Limnos island are well formed, while those from Utah are not curved and rolled up that perfectly and consequently, there are more halloysite surfaces available for $TiO_2$ nanoparticles to be dispersed in the sample from Utah.

In order to investigate the absorption properties of the catalysts, UV–vis reflection spectra were measured and they are shown in Fig. 9. It is observed that the commercial titania P25 showed no absorption in the visible light region. In contrast, the prepared halloysite–$TiO_2$ nanocomposites showed a gray color and absorption in the visible light region, while both samples showed two-step absorption. The calculation of the energy gap at the steep part of the absorption in the UV region and concerning to both materials (pure titania-P25 and composite halloysite/TiO2) showed an $E_g$ = 3.4 eV which is relatively higher compared to theoretical value for the titania-P25 ($E_g$ = 3.2 eV). For the shoulder appear to both halloysite/TiO2 materials, the first absorption should be attributed to $TiO_2$, which was around 410 nm, and the band gap energy could be calculated as 3.0 eV. The second and significantly less pronounced absorption was found around 500 nm (Fig. 9) corresponding to band gap energy of 2.5 eV. This absorption could be attributed to the impurities level caused by carbon doping during the preparation [21]. Both materials show this feature without significant differences between them. The absorption of visible light combined with the well dispersed $TiO_2$ apparently led to the very high activity of the prepared catalysts.

Halloysite serving as a support apparently plays a complex role i.e., it may retard recombination of separated charges generated by UV light irradiation in the crystal lattice of $TiO_2$, thereby increasing catalytic activity. Conversely, halloysite may have a shielding effect, i.e. through scattering or absorbing a certain percentage of the incoming UV light irradiation, decreasing thus the catalytic activity

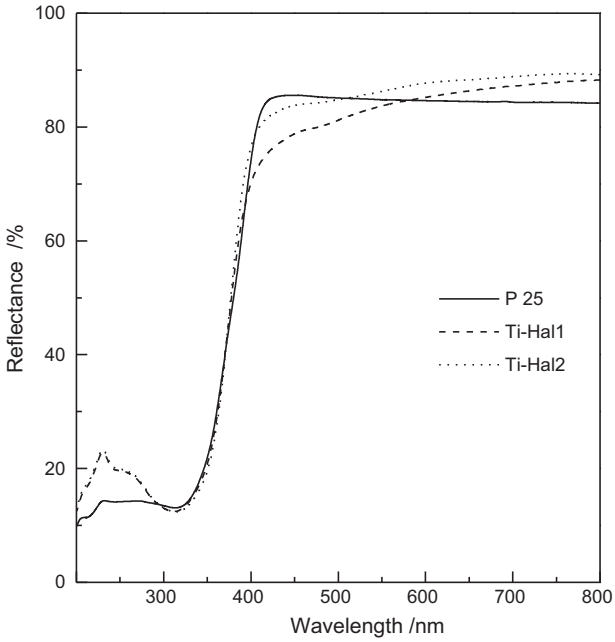


**Fig. 9.** Diffuse reflectance spectra of commercial titania P25 and $TiO_2$-treated halloysite samples (Ti–Hal1 and Ti–Hal2).

[37]. In our case the increased catalytic activity in UV light irradiation (relatively to standard titania) suggests that the shielding effect is not significant. It is evident that dispersion of $TiO_2$ on halloysite surfaces is highly effective for air decontamination (decomposing $NO_x$ and toluene gas) through photocatalytic activity.

## 4. Conclusions

Preparation of halloysite–$TiO_2$ nanocomposites using two different halloysites led to good dispersion of $TiO_2$ on halloysite surfaces. Both halloysites were unaffected by the treatment temperature, while ATR-FTIR results indicated the formation of hydrogen bonding between the outer surfaces of halloysite tubes and $TiO_2$. Both nanocomposites largely showed interparticle mesopores of about 5.7 nm. The prepared halloysite-$TiO_2$ samples showed significantly higher photocatalytic activity in decomposing $NO_x$ gas under visible-light ($\lambda > 510$ nm) and under UV–visible light irradiation ($\lambda > 290$ nm) than that of the commercial titania, P 25. The halloysite-supported $TiO_2$ samples showed also higher toluene vapor photo-oxidation under both UV and sunlight irradiation compared to P25. This higher activity could be attributed to the presence of well-dispersed $TiO_2$ on the halloysite surfaces achieved through the hydrothermal route applied for the synthesis of the $TiO_2$–halloysite nanocomposites.

## Acknowledgments

The authors would like to thank Applied Minerals Inc., New York, USA, for their cooperation and for providing us with halloysite samples. The authors wish to thank Dr. Drakopoulos of the Foundation for Research and Technology-Hellas (FORTH) Institute of Chemical Engineering and High Temperature Chemical Processes (ICE/HT) Rio-Patras, Greece, for his help with SEM micrographs. The research leading to these results has received funding from the European Union's Seventh Framework Programme (FP7/2007-2013) under grant agreement n° 253445. Dr. Christoforidis K.C. acknowledges Marie Curie Action–Intra-European Fellowship (FP7-PEOPLE-2009-IEF-253445) for a Post-doctoral Fellowship.

## References


[1] A. Mills, S. Le Hunte, Journal of Photochemistry and Photobiology 108 (1997) 1–35.
[2] M. Pelaez, A.A. de la Cruz, E. Stathatos, P. Falaras, D.D. Dionysiou, Catalysis Today 144 (2009) 19–25.
[3] Y. Zhang, H. Gan, G. Zhang, Chemical Engineering Journal 172 (2011) 936–943.
[4] S.M. Saqer, D.I. Kondarides, X.E. Verykios, Applied Catalysis B: Environmental 103 (2011) 275–286.
[5] M. Stylidi, D.I. Kondarides, X.E. Verykios, Applied Catalysis B: Environmental 47 (2004) 189–201.
[6] X.B. Chen, S.S. Mao, Chemical Reviews 107 (2007) 2891–2959.
[7] Y.J. Chen, D.D. Dionysiou, Applied Catalysis B: Environmental 80 (2008) 147–155.
[8] D. Zhao, J. Zhou, N. Liu, Materials Science and Engineering: A 431 (2006) 256–262.
[9] M.R. Hoffmann, S.T. Martin, W. Choi, D.W. Bahnemann, Chemical Reviews 95 (1995) 69–96.
[10] S.I. Nishimoto, B. Ohtani, H. Kajiwara, T. Kagiya, Journal of the Chemical Society, Faraday Transactions 181 (1985) 61–68.
[11] M. Fernández-García, A. Martínez-Arias, J.C. Hanson, J.A. Rodriguez, Chemical Reviews 104 (2004) 4063–4104.
[12] A. Fujishima, N.R. Tata, A.T. Donald, Journal of Photochemistry and Photobiology C 1 (2000) 1–21.
[13] M.J. Martínez-Ortiz, G. Fetter, J.M. Domínguez, Microporous and Mesoporous Materials 58 (2003) 73–80.
[14] C. Ooka, H. Yoshida, K. Suzuki, T. Hattori, Applied Catalysis A 260 (2004) 47–53.
[15] S.M. Sun, Y.S. Jiang, L. Yu, F.F. Li, Z.W. Yang, T.Y. Hou, D.Q. Hu, M.S. Xia, Materials Chemistry and Physics 98 (2006) 377–381.
[16] A. Nikolopoulou, D. Papoulis, S. Komarneni, P. Tsolis-Katagas, D. Panagiotaras, G.H. Kacandes, P. Zhang, S. Yin, T. Sato, Applied Clay Science 46 (2009) 363–368.
[17] K. Mogyorósi, A. Farkas, I. Dékány, I. Ilisz, A. Dombi, Environmental Science & Technology 36 (2002) 3618–3624.
[18] D. Kibanova, M. Trejo, H. Destaillats, J. Cervini-Silva, Applied Clay Science 42 (2009) 563–568.
[19] D. Kibanova, M. Sleiman, J. Cervini-Silva, H. Destaillats, Journal of Hazardous Materials 211-212 (2012) 233–239.
[20] L. Chmielarz, Z. Piwowarska, P. Kustrowski, B. Gil, A. Adamski, B. Dudek, M. Michalik, Applied Catalysis B 91 (2009) 449–459.
[21] D. Papoulis, S. Komarneni, A. Nikolopoulou, P. Tsolis-Katagas, D. Panagiotaras, G.H. Kacandes, P. Zhang, S. Yin, T. Sato, H. Katsuki, Applied Clay Sciences 50 (2010) 118–124.
[22] L. Chmielarz, Z. Piwowarska, P. Kustrowski, A. Węgrzyn, B. Gil, A. Kowalczyk, B. Dudek, R. Dziembaj, M. Michalik, Applied Clay Sciences 53 (2011) 164–173.
[23] P. Aranda, R. Kun, M.A. Martín-Luengo, S. Letaïef, I. Dékány, E. Ruiz-Hitzky, Chemistry of Materials 20 (2008) 84–91.
[24] D. Karamanis, A.N. Okte, E. Vardoulakis, T. Vaimakis, Applied Clay Sciences 53 (2011) 181–187.
[25] R. Wang, G. Jiang, Y. Ding, Y. Wang, X. Sun, X. Wang, W. Chen, ACS Applied Materials & Interfaces 3 (2011) 4154–4158.
[26] D. Papoulis, S. Komarneni, D. Panagiotaras, A. Nikolopoulou, K.C. Christoforidis, M. Fernandez-Garcia, P. Zhang, S. Yin, T. Sato, Applied Clay Sciences, http://dx.doi.org/10.1016/j.clay.2012.03.003, in press.
[27] R.E. Hester, R.M. Harrison, Volatile Organic Compounds in the Atmosphere, The Royal Society of Chemistry, Cambridge, 1995.
[28] M. Langlet, P. Jenouvrier, A. Kim, M. Manso, M. Trejo-Valdez, Journal of Sol-Gel Science and Technology 26 (2003) 759–763.
[29] M. Anpo, in: S. Anpo, A. Syoichi (Eds.), NTS, Tokyo (2002) ISBN: 4-86043-009-03, p. 9.
[30] A. Fuerte, M.D. Hernández-Alonso, A.J. Maira, A. Martínez-Arias, M. Fernández-García, J.C. Conesa, J. Soria, G. Munuera, Journal of Catalysis 212 (2002) 1–9.
[31] K.C. Christoforidis, S.J.A. Figueroa, M. Fernández-García, Applied Catalysis B: Environmental 117–118 (2012) 310–316.
[32] G.W. Brindley, K. Robinson, Transactions of the Faraday Society 42B (1946) 198–205.
[33] E. Joussein, S. Petit, J. Churchman, B. Theng, D. Righi, B. Delvaux, Clay Minerals 40 (2005) 383–426.
[34] I. Bobos, J. Duplay, J. Rocha, C. Gomes, Clays and Clay Minerals 49 (2001) 596–607.
[35] K.S.W. Sing, D.H. Everett, R.A.W. Haul, L. Moscou, R.A. Pierotti, N. Rouquerol, T. Siemieniewska, Pure and Applied Chemistry 57 (1985) 603–619.
[36] K.S.W. Sing, R.T. Williams, Particle & Particle Systems Characterization 21 (2004) 71–79.
[37] R. Kun, K. Mogyorósi, I. Dékány, Applied Clay Science 32 (2006) 99–110.